BULLETIN OF CHEMICAL AND PHARMA RESEARCH

Bull. Chem. Pharma Res., **2018**, *2(1)*, 49–56.

www.bcprjournal.com Research Article

Influence of Ce^{3+} Substitution on the Structural and Photocatalytic Properties of Nickel ferrite ($NiFe_{0.5}Ce_{1.5}O_4$) Nanophotocatalysts for degradation of Azocarmine-G Dye

Hemalatha Parangusan[a], Omar Aljarod[a], Deepalekshmi Ponnamma[a]* and Mariam Al Ali AlMaadeed[a,b]

[a]Center for Advanced Materials, Qatar University, P O Box 2713, Doha, Qatar.

[b]Materials Science & Technology Program (MATS), College of Arts & Sciences, Qatar University, Doha 2713, Qatar.

Published Online 19 03 2018

Nickel ferrite and cerium substituted nickel ferrite nanoparticles were synthesized by co-precipitation method. The structural, morphological, optical and photocatalytic properties were investigated. The crystallite size was found to decrease by the substitution of cerium ions in the nickel ferrite. Characteristic UV-Vis absorption data showed red shift for the cerium substituted sample with spherical morphology. Presence of Fe 2p, Ni 2p, and O 1s levels with higher intensities were observed for the cerium substituted nickel ferrite as evidenced from its XPS spectrum. In the presence of normal sunlight the photodegradation efficiencies of synthesized nanoparticles were investigated using the Azocarmine G dye. The cerium substituted nickel ferrite nanoparticles showed higher photocatalytic activity for dye degradation than pure nickel ferrite. This enhanced photocatalytic activity is correlated to the smaller particle size and higher optical absorption property.

INTRODUCTION

Nanotechnology is now considered to be one of the most promising technology in protecting the environment by offering different techniques such as biodegradation, recycling, preventing corrosion and treating waste from the industry.[1-7] Environmental problems associated with water pollutants can cause serious threats to human life. For the last few decades, various physical, chemical and biological techniques as well as photocatalysis are applied to remove pollutants from the waste water.[8-12] In addition to removing the pollutant particles from water, it is equally important to keep the non-toxicity of materials being used and the safety of the method employed. Among various water purification technologies, photocatalysis is a promising technique for the degradation of organic pollutants in water.[13,14] The photocatalysis involves a catalytic reaction by a catalyst with light absorption. This method has several advantages since it deals with catalyst particles of larger surface area, and the availability of light source used.[15]

The most commonly employed photocatalysts are ZnO, TiO_2, WO_3 and SnO_2, due to their non-toxicity, low cost and insolubility under most of the environmental conditions.[16,17] However, the activity of these metal oxide photocatalysts is reduced because of their inability to harvest sunlight efficiently.[18,19] Also, the use of slurry reactor is still limited due to the difficulty for separating nanoparticles from treated water. Recently researchers have been proposed an efficient method of nanoparticle separation from the treated water by using magnetically separable photocatalysts.[20-22] Various magnetic nanoparticles are synthesized based on Fe, Co and Ni for these purposes. $NiFe_2O_4$is a magnetic nanomaterial possessing excellent characteristics such as an inverse spinel structure, high electrical resistivity, high Curie temperature and environmental stability.[23]

The present paper aims to develop magnetically separable photocatalysts based on $NiFe_2O_4$with high photocatalytic activity under visible light irradiation. Synthesis of $NiFe_2O_4$ and Nd substituted $NiFe_2O_4$ photocatalysts by co-precipitation method was exposed extensively by Harish et al.,[24] studying the photocatalytic properties of the material towards

various dyes such as rose Bengal, methylene blue, methyl orange, rhodamine B and methyl red. Here we report the synthesis of $NiFe_2O_4$ and Ce- substituted $NiFe_2O_4$ photocatalysts by co-precipitation. We investigate the importance of cerium substitution in regulating the properties of $NiFe_2O_4$ and substantiate the effect of Cerium substitution in enhancing the photocatalytic activity. AzocarmineG (Azo G) dye was selected as the model dye since it accounts for almost 80% annual production of commercial dye. The prepared photocatalysts were characterized to find their structural, morphological, optical and photocatalytic properties using XRD, FTIR, and SEM with energy dispersive X-ray analysis, UV-Visible absorption spectroscopy (UV-Vis) and XPS. Photodegradation was monitored in regular intervals of time and the influence of concentration of the dye as well as the photocatalysts on the degradation process was studied.

MATERIALS AND METHODS

Chemicals

Nickel acetate ($C_4H_6NiO_4$), Iron (III) Chloride hexahydrate ($FeCl_36H_2O$) and Cerium (III) chloride -7hydrate were purchased from Breckland Scientific Suoolies, U.K.; NaOH, oleic acid and ethanol were obtained from Sigma Aldrich. All reagents in this work were used without any further purification.

Synthesis of Nickel ferrite and Cerium Substituted Nickel ferrite Nanoparticles

Both $NiFe_2O_4$and Ce-substituted $NiFe_2O_4$nanoparticles were prepared following co-precipitation method.[24,25] The starting materials were nickel acetate [$Ni(CH_3COO)_2.2H_2O$] ferric chloride and cerium (III) chloride -7hydrate. The chemicals were taken according to the molecular formula, $NiFe_{2-x}Ce_xO_4$ [where x=0.0, 1.5], and each material was weighed and dissolved in deionized water and mixed together by magnetic stirring. 3M NaOH was added dropwise to the solution to maintain the pH at 13.2. Finally, 3 drops of oleic acid (used as the surfactant)was added to the solution and the whole solution was subjected to a chemical reaction at 80°C temperature for 60min under stirring. After completion of the reaction, the precipitate was washed with distilled water and ethanol, and dried at 80°C in a hot air oven for 3h. Later calcination was done in a tube furnace at 400°C for 2h to obtain the cerium substituted nickel ferrite nano powders. The Ce-substituted $NiFe_2O_4$ was optimized for the best molecular ratio and labelled as $NiFe_{0.5}Ce_{1.5}O_4$.

Characterization Techniques

Sample morphology of the synthesized powders was examined using scanning electron microscope (SEM, XL-30E Philips Co., Holland) and transmission electron microscope (FEI TECNAI G² TEM). XRD diffractometer (Mini Flex 2, Rigaku equipped with Nickel filtered CuKα radiation ($\lambda = 0.1564$ nm) operated at 30 V and 15 mA in the 2θ range of 10-30° at a scanning speed of 1.8°/min), X-ray photoelectron spectroscope (AXIS Ultra DLD XPS) and FT-IR spectroscope (PerkinElmer Spectrum 400 spectrophotometer in the range 400-4000 cm^{-1} with a resolution of 2 cm^{-1}) were used to elucidate the structure of the particles. Photocatalytic activity of $NiFe_2O_4$ and Ce- substituted $NiFe_2O_4$was evaluated by measuring the decolorization rates of Azo G dye. Fig. 1 represents the structure of the commercial organic Azo G. After optimization of the dye concentration, 50ml Azo G and 0.09g of catalysts were mixed in a dark room to maintain adsorption and desorption equilibrium. Thereafter, the samples were kept under normal sunlight on sunny days between 10 a.m. and 2.30 p.m. During this time, the sky was clear, and the rays were very intense in the premises of Qatar University. At given time intervals, the concentration of AzoG dye solution was analysed by a UV spectrophotometer in the range of 200-800nm.

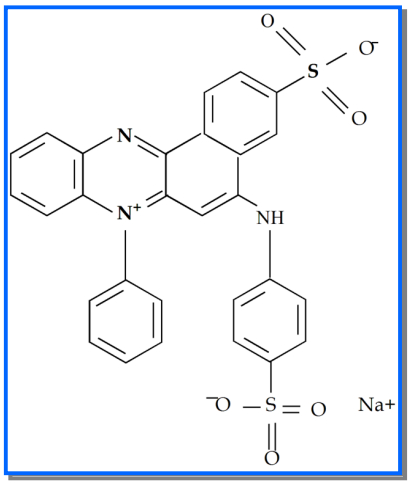

Figure 1. Chemical structure of Azo G dye.

The photocatalytic degradation (PCD) efficiency towards the degradation of Azo G organic dye using the catalyst was estimated as follows:

$$(\%)Degradation = \frac{C_0 - C_t}{C_0} X\ 100 \qquad (1)$$

Where C_t is the concentration of the dye after irradiation of light at a specific time and C_0 the initial dye concentration.[26]

RESULTS AND DISCUSSION

Structural, Thermal and Morphological Studies

Structural investigation of the pure $NiFe_2O_4$ and $NiFe0.5Ce_{1.5}O_4$ nanoparticles was done using the X-ray diffraction patterns as shown in Fig.2. All the diffraction peaks related to the cubic phase of $NiFe_2O_4$with 2θ values of 30.57°, 35.97°, 43.67°, 53.87°, 57.62°, 63.09° and 76.28° corresponding to the crystal phases of (220), (311), (400), (422), (511), (440) and (533) respectively. The obtained XRD diffraction is in accordance with the standard JCPDS pattern [card no –10.0325].[27] In the case of cerium substituted $NiFe_2O_4$, all peaks correspond to the cubic phase of the CeO_2structure

(JCPDS card no. 65-5923). When the cerium ion substituted into the $NiFe_2O_4$, the intensities of cubic phase of the CeO_2grow and the $NiFe_2O_4$ phase becomes disappeared, indicating that the crystallinity of $NiFe_2O_4$ deteriorates and the crystallite size decreases.

The average crystallite sizes of the nanoparticles can be calculated from the Debye Scherrer formula,

$$D = {0.9\lambda}/{\beta cos\theta} \qquad (2)$$

Where, 'D' is the average crystallite size, 'λ' is the wavelength, 'β' is the full-width half maximum and θ is the scattering angle.[28]

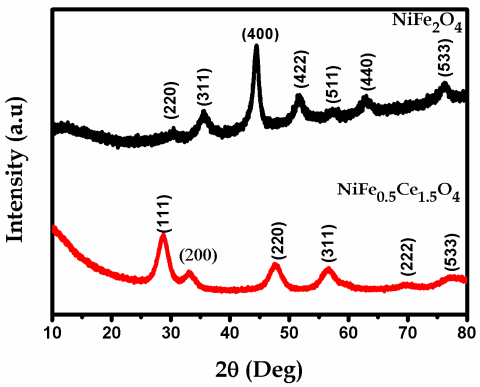

Figure 2. Powder X-ray diffraction pattern for $NiFe_2O_4$and $NiFe_{0.5}Ce_{1.5}O_4$nanostructures.

The average crystallite size for the pure $NiFe_2O_4$was found to be 13 nm, and the substitution of Ce into nickel ferrite lattice caused the further decrease of crystallite size of about 9 nm. The reduction in the crystallite size may be attributed to the distortion in the host lattice by the impurities (i.e., Ce^{3+}) that inhibit the growth of the particle.[29] The lattice parameters for the cubic structured $NiFe_2O_4$ and $NiFe_{0.5}Ce_{1.5}O_4$ nanoparticles were also calculated from the following Equations.

$$2d\ sin\theta = n\lambda \qquad (3)$$

$$d = {a}/{(h^2 + k^2 + l^2)^{1/2}} \qquad (4)$$

Where'd' is the interplanar spacing, 'θ' is the angle of diffraction, 'λ' is the wavelength of X-rays and the h, k, l are the miller indices.[30] For both $NiFe_2O_4$ and $NiFe_{0.5}Ce_{1.5}O_4$ nanoparticles, (311) crystal plane was selected for calculating the lattice parameters. The calculated lattice constants for $NiFe_2O_4$ and $NiFe_{0.5}Ce_{1.5}O_4$ were respectively found to be a= 8.30 and 8.99Å. Here, the lattice parameter was increased with the Ce^{3+} substitution, obeying the Vegard's law.[31] From the XRD results, we conclude that the substitution of Ce ions in the $NiFe_2O_4$ lattice, causes the Ni cations to be replaced with Ce cations. Thus the oxygen atoms in $NiFe_2O_4$ lattice are removed and subsequently oxygen vacancies are produced.[32] This lattice oxygen vacancy was one of the important parameter for the enhancement of photocatalytic activity.

The crystallite size and strain contributions to line broadening are independent of each other and the crystallite size and strain can also be calculated using the Willamson-Hall method.

$$\beta_{total} = \beta_{size} + \beta_{strain} = \left({K\lambda}/{D_{XRD}}\ cos\theta\right) + 4\eta tan\theta \qquad (5)$$

Where λ is the X-ray wavelength, β is the FWHM (full width at half-maximum intensity), θ is the Bragg's angle, and η is the micro strain parameter.[33] The intercept of the plot between ($\beta_{total}\cos\theta/K\lambda$) and $4\sin\theta/K\lambda$is shown in Fig.3. The estimated crystallite sizes of both materials from this method are respectively 15 and 7nm and in good agreement with the values calculated from the Debye-Scherrer formula. The strain is estimated from the slope of the lines which are 2.8×10^{-3} and 3.4×10^{-3}, showing the increased strain value for the Ce substituted $NiFe_2O_4$. This in turn reveals that the lattice imperfections are increased with the Ce substitution which leads to the prevention of $NiFe_2O_4$ crystal growth.

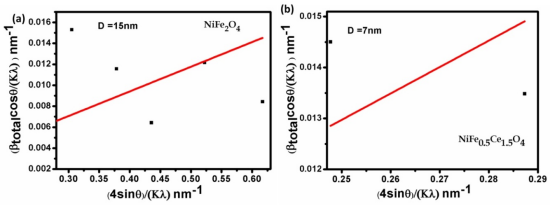

Figure 3. Williamson-Hall plots for $NiFe_2O_4$ and Ce-substituted $NiFe_2O_4$ samples to determine crystallite size and micro strain.

X-ray photoelectron spectroscopy (XPS) was used to analyse the elements present in the samples. The spectrum in Fig. 4a shows the presence of Ni, Fe, O elements in $NiFe_2O_4$with no other elements present.

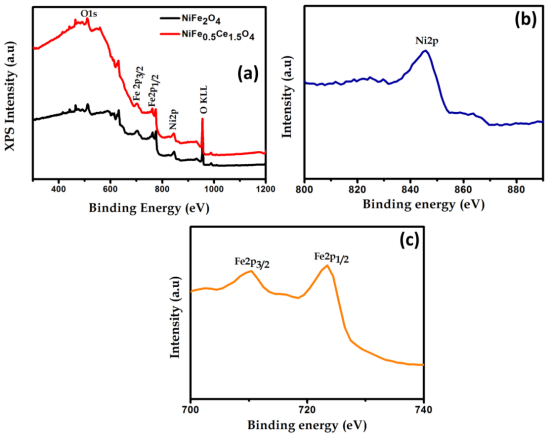

Figure 4. (a) XPS spectra of $NiFe_2O_4$ and $NiFe_{0.5}Ce_{1.5}O_4$, b) Ni 2p region and c) Fe 2p region of $NiFe_2O_4$.

In Fig. 4b, the peak at 848eV binding energy is attributed to the Ni_{2p}. In the spectrum of Fe 2p (Fig. 4c),

the peaks located at 711 and 724eV correspondto the binding energies of $Fe2p_{3/2}$ and $Fe2p_{1/2}$ respectively.[34]
The structural properties of $NiFe_2O_4$ and $NiFe_{0.5}Ce_{1.5}O_4$ samples were further analyzed by FTIR technique as shown in Fig. 5. The absorption bands at 600-500cm^{-1} and 400-470cm^{-1} attribute to the stretching vibrations due to interaction of oxygen and cations in tetrahedral A site and octahedral B site. A broad peak was observed at 3300cm^{-1} and a small peak at 1621cm^{-1}, ascribed to the O-H vibration of water molecules.[35-37] The peak variation of tetrahedral A site is shown in Fig. 5b in which the band position is higher for $NiFe_{0.5}Ce_{1.5}O_4$ than that of pure $NiFe_2O_4$. This can be due to (i) decrease in particle size, (ii) composition of the samples, and (iii) cation substitution causing variation in Ce-oxygen bond length in A-site and B-site.[38,39] It is also found that the absorption band of A site peak position slightly shifts to higher wavenumber side with the substitution of Ce-ions in accordance with the reports of Hemeda and Shinde et al.[40,41]

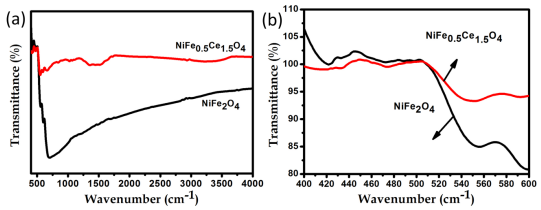

Figure 5. FTIR spectra of $NiFe_2O_4$ and $NiFe_{0.5}Ce_{1.5}O_4$.

Morphological Analysis

The surface morphology of the pure $NiFe_2O_4$ and $NiFe_{0.5}Ce_{1.5}O_4$ are shown in Fig 6. Fig 6(a) shows the morphology for pure $NiFe_2O_4$ illustrating the spherical appearance with less agglomeration. This structure is modified into fine particles which are more or less spherical in shape in $NiFe_{0.5}Ce_{1.5}O_4$ as shown in Fig 6(b).

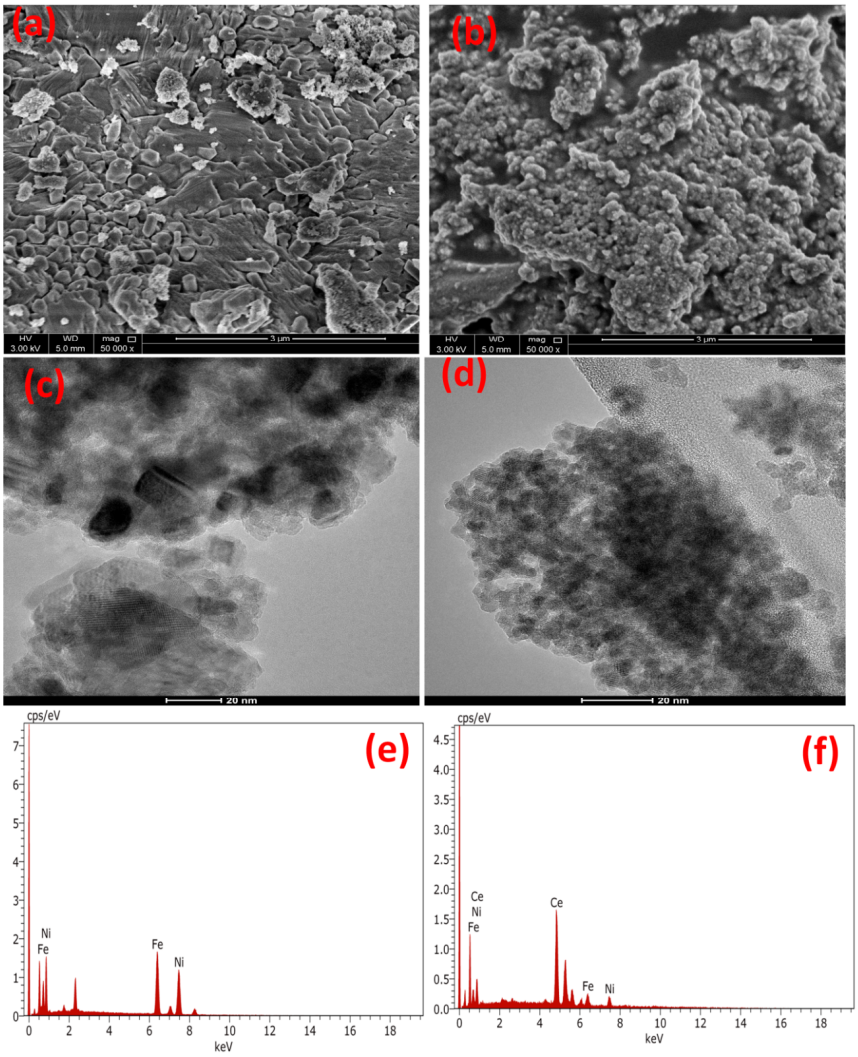

Figure 6. (a,b) SEM images (c, d) TEM images and (e, f) EDAX images of $NiFe_2O_4$ and $NiFe_{0.5}Ce_{1.5}O_4$.

These morphological changes were due to the incorporation of Ce-ions into the $NiFe_2O_4$ lattice. The surface morphology of pure and cerium substituted nickel ferrite samples were further analyzed by the Transmission electron microscopy (TEM) is shown in

Fig. 6(c, d). In Fig 6d, the spherical shaped morphology with less agglomeration was observed for nickel ferrite and cerium substituted nickel ferrites. The elemental analysis spectra of pure $NiFe_2O_4$ and Ce-substituted $NiFe_2O_4$ are shown in Fig.6 (e, f) in which the characteristic peaks of Ni, Fe, O, Ce peaks are found.

UV-Vis Absorption Analysis

Fig. 7 shows the UV-Vis absorption spectra of pure $NiFe_2O_4$ and $NiFe_{0.5}Ce_{1.5}O_4$ nanoparticles. In the UV region a strong peak was observed at a wavelength of around 300nm, attributed to the band gap absorption of $NiFe_2O_4$ nanoparticles. In the visible region, two strong absorption peaks were observed at wavelengths of about 456 and 605nm. The absorptions in the visible region was due to the Fe^{3+} 3d-3d spin forbidden transition (indirect transition).[42] Also, the visible region absorption spectrum exhibits broad spectrum which was mainly attributed to the charge transfer excitations from the O 2p dominated occupied to the Fe 3d character unoccupied valence states or it may be due to the crystalline spinel structure.[43,44] The absorption band was shifted towards higher wavelength side for $NiFe_{0.5}Ce_{1.5}O_4$ nanoparticles. In other words, it shows a red shift. The band gap of the pure $NiFe_2O_4$ and $NiFe_{0.5}Ce_{1.5}O_4$ nanoparticles was determined using the following equation.

$$\alpha h\nu = A\left(h\nu - E_g\right)^n \qquad (6)$$

Where hν is the photon energy, A is the constant relative to the material, α is the absorption co-efficient, λ is the wavelength in nm, E_g is the band gap energy, n = ½ for allowed direct band and 2 for the allowed indirect transition. However, n takes the values of 3/2 and 3 for the direct and indirect forbidden transitions respectively.[45] In order to calculate the E_g values, a graph was plotted between $(\alpha h\nu)^2$ versus photon energy (hν). The intercept on the X-axis gives the band gap of the nanoparticles. These Tauc's plots were shown in Fig. 7 (b, c). The calculated band gap values were 2.2eV and 1.8eV respectively for pure $NiFe_2O_4$ and $NiFe_{0.5}Ce_{1.5}O_4$. It is found that the band gap value decreases for the Ce- substituted sample. In our case, the decrease in band gap value can be attributed to the formation of Ce secondary phases which was consistent with the XRD results.[46] The substitution of Ce-ions into the $NiFe_2O_4$ shows secondary peaks corresponding to the Ce-ions. The reduction in band gap implies the possible application of these nanomaterials in potential visible light driven photocatalysts.

Photocatalytic Degradation of the Organic Pollutant

The photocatalytic activity of pure $NiFe_2O_4$ and $NiFe_{0.5}Ce_{1.5}O_4$ was evaluated by measuring the decolorization rates of the Azo G dye. The effects of photocatalyst dosage and dye concentration were investigated first. The initial dye concentration under visible light irradiation was varied from 10-60ppm and the amount of catalyst and irradiation time was kept constant. The degradation efficiency decreased when the dye concentration increased from 10 to 30ppm. This is due to the lower number of dye molecules presented in the solution and less utilization of OH radicals.[47] The degradation efficiency was higher at 40ppm, due to the presence of enough dye molecules in comparison to OH* radicals for the degradation of dye. Further increase in the concentration of the dye, reduced the PCD efficiency, since higher number of dye molecules in the solution increases the competition with OH* radicals.[48] Therefore, the optimum dye concentration was selected as 40ppm.

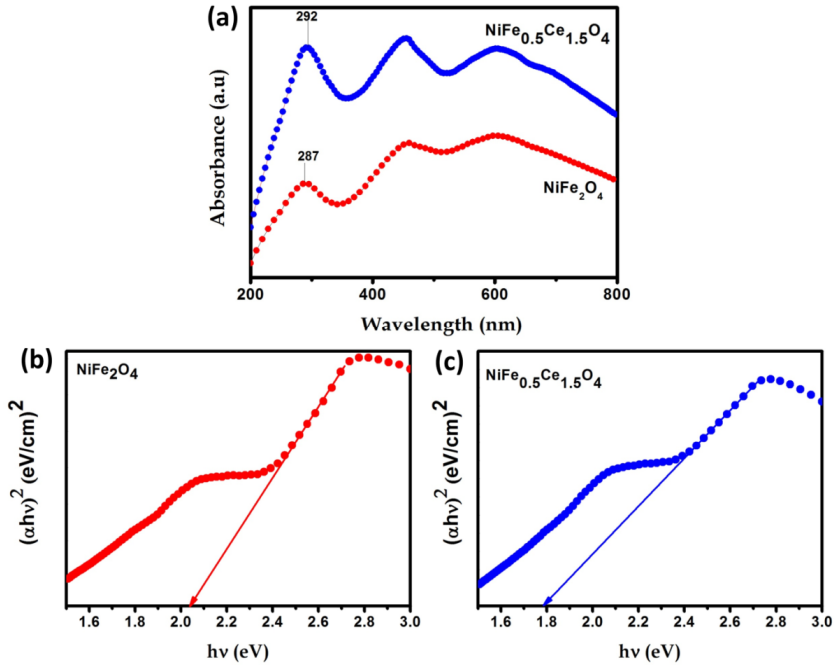

Figure 7. (a) Absorption spectra for $NiFe_2O_4$ and $NiFe_{0.5}Ce_{1.5}O_4$, (b, c) Tauc's plot of $NiFe_2O_4$ and $NiFe_{0.5}Ce_{1.5}O_4$.

The effect of catalyst concentration on the dye degradation is a very significant parameter in regulating the PCD efficiency. Here, the catalyst amount was varied from 10 to 120mg/50ml. The degradation efficiency increased from 10 to 90mg/50 ml and when the amount of photocatalyst enhanced beyond 90 mg, the degradation efficiency was decreased. Here, the strong particle-particle interactions and increased light scattering are the main reasons for the decrease in number of active sites on the photocatalyst surface.[49]

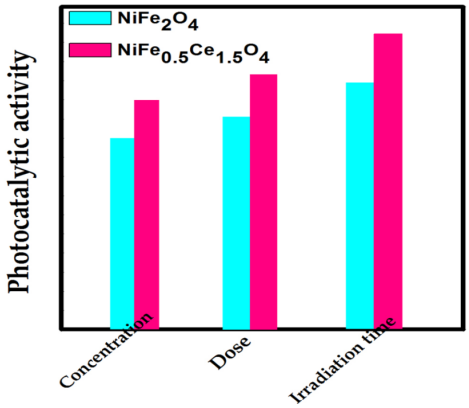

Figure 8. Comparison of the photocatalytic activity of $NiFe_2O_4$ and $NiFe_{0.5}Ce_{1.5}O_4$ nanoparticles.

Fig. 8 shows the comparison of photocatalytic activity of the catalyst by changing different parameters. The results clearly indicate that the $NiFe_{0.5}Ce_{1.5}O_4$ nanoparticles are better catalysts for the degradation of Azo G dye compared to pure $NiFe_2O_4$.

UV-Vis absorption spectrum of Azo G with different reaction time under sun light irradiation in the presence of $NiFe_{0.5}Ce_{1.5}O_4$ catalyst is shown in Fig.9 (a, b). The intensity of the absorption peak diminishes as the irradiation time increases. This indicates the complete degradation of Azo G. The value of C/C_o plotted against time (Fig. 9c) illustrates the higher degradation efficiency for $NiFe_{0.5}Ce_{1.5}O_4$ nanoparticles compared to pure $NiFe_2O_4$. 90% of dye degradation is achieved in the $NiFe_{0.5}Ce_{1.5}O_4$ sample within 120 min.

The photocatalytic activity depends upon a number of factors such as particles size, morphology and surface properties of the photocatalysts.[50-52] Here the higher photocatalytic activity achieved for $NiFe_{0.5}Ce_{1.5}O_4$ can be mainly due to its smaller particle size as evident from the XRD results.

Based on aforementioned studies, a degradation mechanism was proposed for the $NiFe_{0.5}Ce_{1.5}O_4$ photocatalyst for degrading the organic pollutant Azo G under sunlight (Fig. 10). Many reactive species such as hydroxyl (*OH) and superoxide ($*O_2^-$) radicals formed during the reaction play important roles in the degradation of organic dyes.[53]

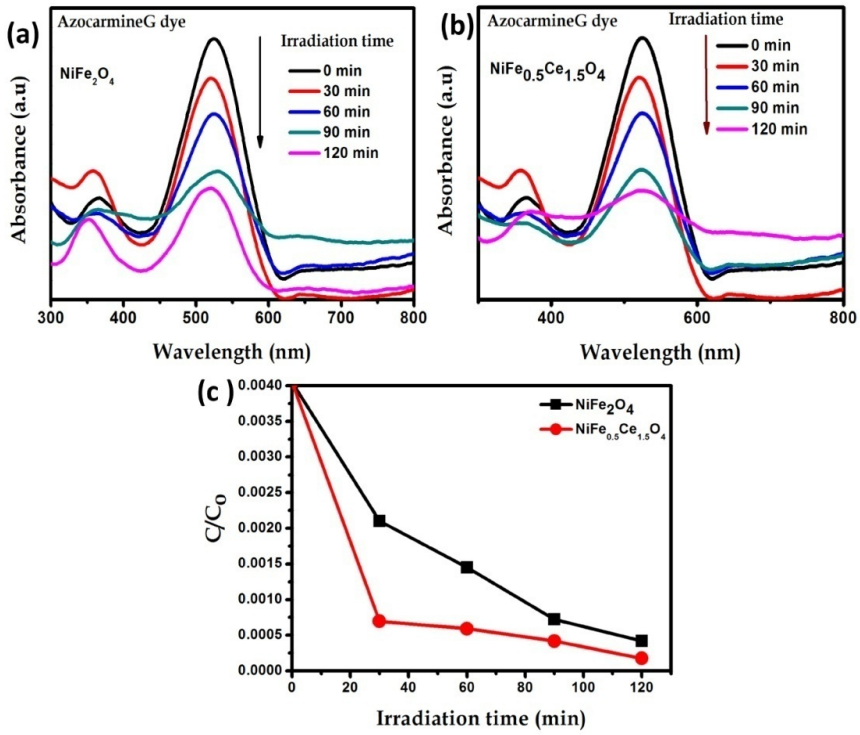

Figure 9. (a, b) UV-visible absorption spectra of the photocatalytic activity of AzoG dye (= 40 ppm, catalyst = 90mg/50ml), (c)plots of C/Co versus irradiation time.

When a photon of energy (hν) equal or higher than the band gap energy of the material is irradiated on the sample, electron-hole pairs are created. These charge carriers act as photocatalytic active centres.[54] The holes in the valence band are oxidized to react with surface water present in the dye to form OH radicals. The electrons in the conduction band reduce the oxygen to give superoxide radicals. These two radicals are the powerful tools in disintegrating the organic pollutants and convert it to mineralized products.[55] The following reaction explains the photodegradation of Azo G dye by $NiFe_{0.5}Ce_{1.5}O_4$ catalyst:

$$NiFe_{0.5}Ce_{1.5}O_4 + h\nu \rightarrow NiFe_{0.5}Ce_{1.5}O_4\,(h^+_{VB}) + NiFe_{0.5}Ce_{1.5}O_4\,(e^-_{CB}) \quad (7)$$

$$NiFe_{0.5}Ce_{1.5}O_4\,(h^+_{VB}) + H_2\,O \rightarrow H^+ + OH^* \quad (8)$$

$$H_2\,O \leftrightarrow H^+ + OH- \quad (9)$$

$$NiFe_{0.5}Ce_{1.5}O_4\,(h^+_{VB}) + OH- \rightarrow OH^* \quad (10)$$

$$NiFe_{0.5}Ce_{1.5}O_4\,(e^-_{CB}) + O_2 \rightarrow O_2^* - \quad (11)$$

$$O_2^{*-} + H^+ \rightarrow HO_2^* \quad (12)$$

$$2e^-_{Cb} + HO_2^* + H^+ \rightarrow OH^* + OH^- \quad (13)$$

$$OH^*, HO_2^*, O_2^{*-} + MB \rightarrow Degradation\ products\ (CO_2, H_2O) \quad (14)$$

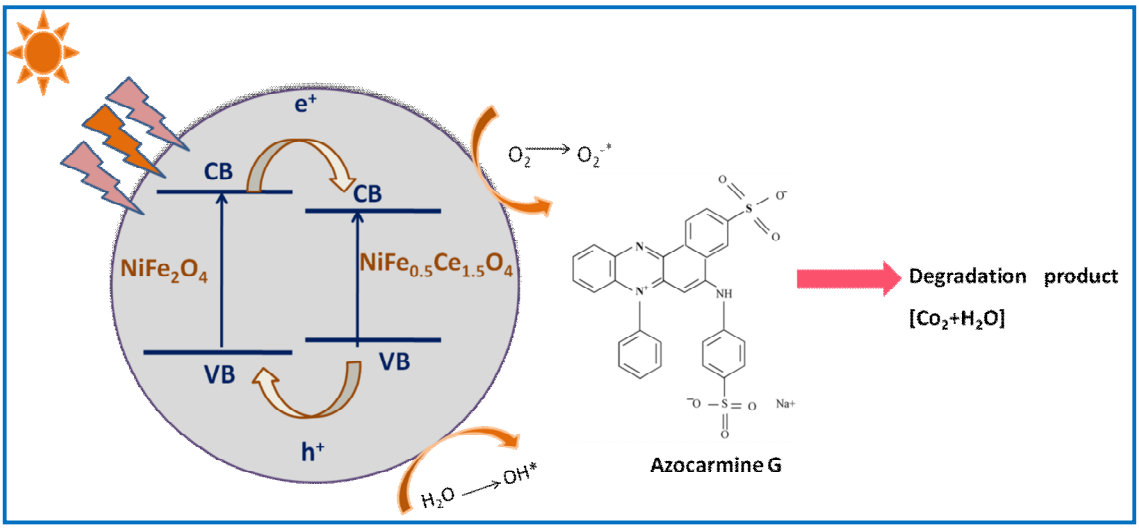

Figure 10. Photocatalytic degradation mechanism of Azo G dye under visible light irradiation.

Conclusions

Pure $NiFe_2O_4$ and $NiFe_{0.5}Ce_{1.5}O_4$ nanoparticles were synthesized by co-precipitation method. The structural characterization reveals the cubic structure of $NiFe_2O_4$ nanoparticles with a crystalline size of 13 nm. With cerium doping this size was reduced to 9nm for $NiFe_{0.5}Ce_{1.5}O_4$. The optical band gap of the Ce-substituted sample showed a red shift when compared with the pure $NiFe_2O_4$. $NiFe_{0.5}Ce_{1.5}O_4$ showed enhanced photocatalytic activity compared to the pure $NiFe_2O_4$ sample due to its smaller crystallite size. The maximum degradation efficiency for Azo G dye degradation was achieved in 120 min, which proves the significance of cerium substituted $NiFe_2O_4$ in photocatalytic degradation of organic pollutants.

Acknowledgements

This publication is made possible by NPRP grant 6-282-2-119 from the Qatar National Research Fund (a member of Qatar Foundation). The statements made herein are solely the responsibility of the authors.

Notes and References

*Corresponding Author Details: *Deepalekshmi Ponnamma Center for Advanced Materials, Qatar University, P O Box 2713, Doha, Qatar.*
E-mail id.: lekshmi_deepa@yahoo.com
† Supporting Information (SI): Not available.

1. K. Deshmukh, M. B. Ahmed, R. R. Deshmukh, S. K. K. Pasha, K. K. Sadasivuni, A. R. Polu, D. Ponnamma, M. A. Al-Maadeed and K. Chidambaram, *J. Mater. Sci.: Mater. Electron.,* **2017**, *28*, 973.
2. M. B. Ghazy, F. A. Esmail, W. K. El-Zawawy, M. A. Al-Maadeed, and M. E. Owda, *J. Adv. Chem.*, **2016**, *12*, 3.
3. D. Ponnamma, P. P. Vijayan and M. A. Al-Maadeed, *Mat. Des.*, **2017**, *117*, 203.
4. M. A. Al-Maadeed, Y. M. Shabana and P. N. Khanam, *Mater. Des.*, **2014**, *581*, 374.
5. E. M. Fayyad, K. K. Sadasivuni, D. Ponnamma and M. A. Al-Maadeed, *Carbohyd. Polym.*, **2016**, *151*, 871.
6. M. Rajan, M. Murugan, D. Ponnamma, K. K. Sadasivuni and M. A. Munusamy, *Biomedicine & Pharmacotherapy*, **2016**, *83*, 201.
7. A. M. Abdullah, A. A. Mohamed, A. Bahgat and M. A. Al-Maadeed, *ECS Trans.*, **2015**, *64*, 57.
8. Y. He, *Chin. Particuol.*, **2004**, *2*, 168.
9. C. Hu and Y. Z. Wang, *Chemosphere*, **1999**, *39*, 2107.
10. J. Kiwi, C. M. Pulgarine and P. P. Gratzel, *Appl. Catal. B.: Environ.*, **1993**, *3*, 85.
11. J. Li, Y. Xu, Y. Liu, D. Wu and Y. Sun, *Chin. Particuol.*, **2004**, *2*, 266.
12. M. R. Hoffman, S. T. Martin, W. Choi and D. W. Bahnemann, *Chem. Rev.*, **1995**, *95*, 69.
13. H. Parangusan, D. Ponnamma, M. A. Al-Maadeed and A. Marimuthu, *Photochemistry and photobiology,* **2018**, *94*, 237.
14. R. Vinu and G. Madras, *J. Indian Inst. Sci.*, **2010**, *90*, 189.
15. V. Parmon, A. V. Emeline and N. Serpone, *J. Photochem. Photobiol. A Chem.*, **2002**, *4*, 91.
16. S. S. Shinde, C. H. Bhosale and K. Y. Rajpure, *J. Photochem. Photobiol.*, **2012**, *B 113*, 70.
17. J. V. Sanchez, J. P. P. Orozco, R. S. Parra and I. H. Perez, *Rev. Mex. Ing. Quim.*, **2012**, *11*, 121.
18. H. Katsumata, Y. Oda, S. Kanecoa and T. Suzukib, *RSC Adv.*, **2013**, *3*, 5028.
19. S. M. Lam, J. C. Sin, A. Z. Abdullah and A. R. Mohamed, *Sep. Purif. Technol.*, **2014**, *132*, 378.
20. X. U. Shihong, S. Wenfeng, Y. Jian, C. Mingxia and S. Jianwei, *Chin. J. Chem. Eng.*, **2007**, *15*, 190.
21. D. Beydoun, R. Amal, G. Low and S. McEvoy, *J. Phys. Chem. B*, **2000**, *104*, 4387.
22. D. Beydoun, R. Amal, J. Scott, G. Low and S. McEvoy, *Chem. Eng. Technol.*, **2001**, *24*, 745.
23. Y. Kinemuchi, K. Ishizaka, H. Suematsu, W. H. Jiang and K. Yatsui, *Thin Solid Films*, **2002**, *407*, 109.
24. K. N. Harish, H. S. Bhojya Naik, P. N. Prashanthkumar and R. Viswanath, *ACS Sustainable Chem. Eng.*, **2013**, *1*, 1143.
25. K. Maaz, S. Karim, A. Mashiatullah, J. Liu, M. D. Hou, Y. M. Sun, J. L. Duan, H. J. Yao, D. Mob and Y. F. Chen, *J. Magn. Magn. Mater.*, **2009**, *321*, 1838.
26. S. Das, A. Samanta and S. Jana, *ACS Sustainable Chem. Eng.*, **2017**, DOI: 10.1021/acssuschemeng.7b02003.
27. S. Qu, J. Wang, J. L. Kong, P. Y. Yang and G. Chen, *Talanta.*, **2007**, *71*, 1096.
28. C. Hammond, *The Basics of Crystallography and Diffraction*, Oxford University Press, Oxford, **1997**.
29. N. Rajeswari Yogamalar and A. Chandra Bose, *Appl. Phy. A.*, **2011**, *103*, 33.
30. G. Dixit, J. P. Singh, C. L. Chen, C. L. Dong, R. C. Srivastava, H. M. Agrawal, W. F. Pong and K. Asokan, *J. Alloys Compd.*, **2013**, *581*, 178.
31. H. L. Shi and Y. Duan, *Eur. Phys. J.*, **2008**, *B.66*, 493.
32. H. E. Liying, S. U. Yumin, J. Lanhong and S. H. I. Shikao, *J. Rare Earths*, **2015**, *33*, 791.
33. G. Anandhababu, G. Ravi, T. Mahalingam, M. Navaneethan, M. Arivanandham and Y. Hayakawa, *J. Phys. Chem. C*, **2014**, *118*, 23335.
34. M. Fu, Q. Jiao and Y. Zhao, *J. Mater. Chem. A.*, **2013**, *1*, 5577.
35. L. Zhao, H. Yang, X. Zhao, L. Yu, Y. Cui and S. Feng, *Mater. Lett.*, **2006**, *60*, 1.
36. M. Mazaheri, S. A. Hassanzadeh-Tabrizi, M. Aminzare and S. K. Sadrnezhaad, *Proceedings of the 11th ECERS Conference*, Krakow, **2009**, p. 655.
37. G. Dixit, J. P. Singh, R. C. Srivastava and H. M. Agrawal, *J. Magn. Magn. Mater.*, **2013**, *345*, 65.
38. G. Umapathy, G. Senguttuvan, L. John Berchmans, V. Sivakumar and P. Jegatheesan, *J. Mater. Sci.: Mater. Electron.*, **2017**, *28*, 17505.
39. M. L. Dos Santos, R. C. Lima, C. S. Riccardi, R. L. Tranquilin, P. R. Bueno, J. A. Varela and E. Longo, *Mater. Lett.*, **2008**, *62*, 4509.
40. O. M. Hemeda, M. M. Barakat and D. M. Hemeda, *J. Phys.*, **2004**, *27*, 537.
41. T. J. Shinde, A. B. Gadkari and P. N. Vasambekar, *J. Alloys Compd.*, **2012**, *513*, 80.
42. R. Suresh, K. Giribabu, R. Manigandan, A. Stephen and V. Narayanan, *RSC Adv.*, **2014**, *4*, 17146.
43. A. Sutka, T. K¨ambre, R. P¨arna, N. D¨obelin, M. Vanags, K. Smits and V. Kisand, *RSC Adv.*, **2016**, *6*, 18834.
44. D. Hong, Y. Yamada, M. Sheehan, S. Shikano, C. H. Kuo, M. Tian, C. K. T. Sung and S. Fukuzumi, *ACS Sustainable Chem. Eng.*, **2014**, *2*, 2588.
45. J. I. Panvoke, *Optical Process in Semiconductors* (Prentice-Hall), New Jersey, **1971**.
46. S. Suwanboona, P. Amornpitoksukb, A. Sukolrat and N. Muensit, *Ceram. Int.*, **2013**, *39*, 2811.
47. Priyanka and V. C. Srivastava, *Ind. Eng. Chem. Res.*, **2013**, *52*, 17790.
48. M. S. Lucas and J. A. Peres, *Dyes Pigm.*, **2006**, *71*, 236.
49. S. K. Pardeshi and A. B. Patil, *J. Mol. Catal. A.*, **2009**, *308*, 32.
50. M. S. Tomar, R. Melgarejo, P. S. Dobal and R. S. Katiyar, *J. Mater. Res.*, **2001**, *16*, 903.
51. D. Li and H. Haneda, *Chemosphere*, **2003**, *51*, 129.
52. L. Q. Jing, Z. L. Xu, X. J. Sun, J. Shang and W. M. Cai, *Appl. Surf. Sci.*, **2001**, *180*, 308.
53. S. M. Wang, D. L. Li, C. Sun, S. G. Yang, Y. Guan and H. He, *Appl. Catal. B.*, **2014**, *144*, 885.
54. P. Hemalatha, S. N. Karthick, K. V. Hemalatha, Moonsuk Yi, Hee-Je Kim and M. Alagar, *J. Mater. Sci.: Mater. Electron.*, **2016**, *27*, 2367.
55. L. Zhang, X. Zhou, X. Guo, X. Song and X. Liu, *J. Mol. Catal. A: Chem.*, **2011**, *335*, 31.